

Petter Ekman

Department of Management and Engineering,
Linköping University,
Linköping 58183, Sweden
e-mail: petter.ekman@liu.se

James Venning

Department of Mechanical and
Aerospace Engineering,
Monash University,
Clayton 3800, Victoria, Australia
e-mail: mail@jamesvenning.net

Torbjörn Virdung

Volvo Car Corporation Department,
PO Box PVT2 SE-405 31,
Göteborg 91380, Sweden
e-mail: torbjorn.virdung@volvocars.com

Matts Karlsson

Department of Management and Engineering,
Linköping University,
Linköping 58183, Sweden
e-mail: matts.karlsson@liu.se

Importance of Sub-Grid Scale Modeling for Accurate Aerodynamic Simulations

The Ahmed body is one of the most well-investigated vehicle bodies for aerodynamic purposes. Despite its simple geometry, the flow around the body, especially at the rear, is very complex as it is dominated by a large wake with strong interaction between vortical structures. In this study, the flow around the 25 deg Ahmed body has been investigated using large eddy simulations and compared to high-resolution particle image velocimetry (PIV) measurements. Special emphasis was put on studying three commonly used sub-grid scale (SGS) models and their ability to capture vortical structures around the Ahmed body. The ability of the SGS models to capture the near-wall behavior and small-scale dissipation is crucial for capturing the correct flow field. Very good agreement between simulations and PIV measurements were seen when using the dynamic Smagorinsky-Lilly and the wall-adopting local eddy-viscosity SGS models, respectively. However, the standard Smagorinsky-Lilly model was not able to capture the flow patterns when compared to the PIV measurements due to shortcomings in the near-wall modeling in the standard Smagorinsky-Lilly model, resulting in overpredicted separation.

[DOI: 10.1115/1.4048351]

1 Introduction

Reducing fuel consumption and emissions are among the main challenges for the transport sector. The aerodynamic drag can be responsible for 30–80% of the total resistance for a vehicle traveling at highway speed, depending on vehicle type and road conditions [1]. Thus, the aerodynamic drag has a major effect on the energy consumption and emissions. However, the flow around a vehicle does not only affect the performance of the vehicle, but also the safety and comfort of the vehicle [1].

A large portion of the drag is produced by the rear end of the vehicle. The bluff body has the ability to capture similar behavior of the flow around a vehicle, and makes it possible to use more generalized shapes to study parameters affecting the flow. Due to this, the use of bluff bodies for computational fluid dynamics (CFD) studies have been, and is still, widely used. Especially, for scale-resolving simulations (SRS), where use of fine near-wall meshes may be important.

One of the most studied bluff bodies is the Ahmed body, introduced in 1984 by Ahmed et al. [2]. This bluff body is a simplified vehicle model consisting of a rounded front, a long midsection and a box shaped rear end with a top slant; in the original configuration supported from the ground by four circular cylinders, one in each corner. The body was created for emphasizing the effect on the time-averaged wake structures and how it affects the drag of such a basic vehicle type [2]. Despite the simplified geometry, the flow around the body, especially at the rear, is very complex due to the slanted top at the rear of the body causing several important vortical structures in the wake. The slant angle has a significant impact on the drag, as these vortical structures are directly affected by it. In Ref. [2] it was seen that the majority of the drag was caused by the low-pressure distribution at the slant and base of the body. Previous studies have also shown that the wake structures change dramatically for a slant angle of about 30 deg [2–6].

For a slant angle less than 30 deg, however, Ahmed et al. [2] noticed that a separating shear layer turns outward from the sides

of the edges of the slant (C-pillar) and rolls into two longitudinal vortices, which dominate the behavior of the wake. Furthermore, the flow separates over the sharp edge where the roof and slant meet and creates an arch-shaped separation bubble. The length of this separation bubble has been seen to be dependent on the Reynolds number when comparing different experimental studies, see, e.g., Refs. [7] and [8]. For moderate and higher Reynolds numbers the flow reattaches along the slant, but for low Reynolds numbers (i.e., less than $Re_L = 3 \times 10^4$) the separation never reattaches [9].

For slant angles close to 30 deg the size of this separation grows and causes a low pressure at the center of the slant. This low pressure affects the C-pillar vortices by making them stronger, which endorse the reattachment. Behind the base two larger vortical structures occurs, forming a large recirculating flow region behind the body. Sims-Williams et al. [3] noted that the behavior of the wake suddenly can change from a closed separation bubble to fully separated flow over the slant, for a slant angle of 30 deg. It was also seen that it was possible to initiate the different states by guiding the flow onto the slant or force it to separate. For higher Reynolds numbers ($Re_L = 6.2 \times 10^5$) the reattaching state was more stable. The highest drag occurs for this slant angle when the flow remains in the closed separation bubble state [2,6,10].

For a slant angle over 30 deg the flow separates over the whole slant and joins the C-pillar vortices, creating a large wake behind the body [2–4] and reducing drag [1].

The 25 deg slant angle has been investigated in several studies at several different Reynolds numbers. Lienhart and Becker [4] noted that for the 25 deg, at a higher Reynolds number ($Re_L = 2.86 \times 10^6$), that the flow mainly stayed attached over the center of the slant. However, a small separation zone directly after the slant edge was noted. The two counter-rotating C-pillar vortices were deemed the reason for the attached flow, even up to a slant angle of approximately 30 deg. It was also seen that these C-pillar vortices extended more than 0.5 body lengths, L , behind the body [4].

Venning et al. [8], published in 2015 a study where extensive high-resolution particle image velocimetry (PIV) measurements were performed at the rear of the Ahmed body with a slant angle of 25 deg. The measurements were made in a water tunnel with low freestream velocity, resulting in a Reynolds number of $Re_L = 9.34 \times 10^4$, almost 46 times lower than the original study

Contributed by the Fluids Engineering Division of ASME for publication in the JOURNAL OF FLUIDS ENGINEERING. Manuscript received April 24, 2019; final manuscript received July 20, 2020; published online October 13, 2020. Assoc. Editor: Ioannis K. Nikolos.

made by Ahmed et al. [2]. Venning et al. [8] especially studied the behavior of the C-pillar vortices and corner vortices at the lower part of the body, and how these were affected by the width of the body. These vortices have, as earlier mentioned, a huge impact on the behavior of the wake and hence the flow characteristics of the body. Leclerc [11] showed that 12%, 34%, and 44% of the drag are caused by the C-pillar vortices, separation bubble on the slant and the three-dimensional (3D) wake behind the rear base of the body, respectively. Thacker et al. [7] could also demonstrate that the location of the center of the vortical structures in the separation bubble at the slant and in the 3D wake had a significant effect on the pressure distribution, and hence the aerodynamic forces. This has also been seen for other geometries with a slanted rear, such as the Davis body studied by Fuller and Passmore [12], where the effect of changing the geometry of the C-pillar had a direct effect of the C-pillar vortices, wake structures and surface pressure distribution. Several studies have also shown this to be true for more realistic fastback and notchback geometries, see, e.g., Refs. [13–16]. All these findings show the importance of capturing these vortices and wake structures accurately.

Due to the simplistic shape but still complex flow characteristics of the Ahmed body, it has also become a popular test case within the CFD community.

Several studies exist where Reynolds-averaged Navier–Stokes (RANS) turbulence models have been applied for simulating the flow around the Ahmed body [10,17–21]. These studies used a large variety of models ranging from classical two-equation models to more advanced Reynolds stress models. It could be seen that the RANS models are able to capture the wake behavior of the 35 deg slanted body well, while missing important features for the 25 deg slant angle [19–21]. The main reason why the RANS model struggle to capture the behavior for the flow over the slant is that the RANS models are not able to accurately model the behavior of the small-scale structures of the separated region [22]. These small structures have a significant influence on the increase of the momentum transfer across the mean streamlines and does increase the unsteadiness and the 3-dimensionality of the flow [22,23]. This in turn also increase the unsteady behavior of the wake.

Hybrid RANS large eddy simulation models (LES), where the near-wall flow is modeled, in order to not resolve the boundary layer, have been applied to simulate the flow around the body [21,22,24]. As these approaches often also use a RANS model for the near-wall flow, they struggle to accurately capture the wake. Improvements have been seen for the general wake behavior compared to RANS simulation, but hybrid RANS-LES models seem still to have problems to predict the mild separation and reattachment on the slant, causing effects on the behavior of the wake and pressure distribution [22]. However, some improvements have recently been seen when using the improved delayed detached eddy simulation (IDDES) model [25]. Specifically, the velocity distribution at the separated region at the center of slant is clearly improved with the IDDES model when compared to a detached eddy simulation model.

A number of LES studies have been made on the Ahmed body, with different sub-grid scale models and near-wall treatments [22,23,26–29]. Most of these studies investigated the flow around the body at a higher Reynolds number, causing high demands for large mesh sizes to reach the necessary mesh resolution, which may not always been achieved [21,22].

Utilizing the flow field insensitivity with respect to the Reynolds number, over the rear of the Ahmed body, as used in the high-resolution PIV measurements performed by Venning et al. [8] and [30], makes it well suited for further comparative studies of LES predictability.

In order to improve the accuracy of CFD simulations, and as computational power is becoming more available, use of more SRS is occurring, especially in the automotive industry. These SRS methods most often uses SGS models to model the behavior and effect of the smallest scales within the LES region.

In this study, three frequently used LES SGS models are compared to these high-resolution PIV measurements in order to investigate the effects of the different SGS models. The effect of the SGS modeling of the smaller scales is supposed to have small effects of the overall flow field. However, some studies of external flows have shown that the SGS modeling can cause significant differences [31,32]. The flow around the Ahmed body have already been investigated with different SGS models [22,23,26–29], but in different studies with different numerical schemes, meshes and configurations, making it difficult to make any direct comparison. Hence, there is a need to understand and investigate how different LES SGS models affect the flow around the Ahmed body. Here, we investigate, three frequently used SGS models, the Smagorinsky-Lilly (SM) model, the dynamic Smagorinsky-Lilly model (DSM) and the wall-adapting local eddy-viscosity (WALE) model, and their impact on the flow around the 25 deg Ahmed body when compared with high-resolution PIV data. The results focus on the ability and accuracy of these SGS models to capture the main vortical structures over the slant and in the wake of the body and their suitability for simulating the flow around ground vehicles.

2 Method

2.1 Geometry. The geometry used in this study is based on the well-known Ahmed body, introduced by Ahmed et al. in 1984 [2]. However, to be able to directly compare simulations with the available high-resolution PIV measurements performed in Refs. [8] and [30], the body follows the configuration of these experiments: supported on two NACA0030 stilts with a chord length of $0.79H$ and height of $0.17H$, respectively, where H is the height of the body and equals 72.3 mm. The length, L , and width, W , of the model is 261 mm and 97.3 mm, respectively. The stilts are positioned such that the distance from the leading vertical surface of the body to the leading edge of the front and rear stilts are $0.56H$ and $2.2H$, respectively. An illustration of the body can be seen in Fig. 1. Only the 25 deg slant angle is investigated with a slant length, L_{slant} , of $0.77H$. The origin of the coordinate system is defined at the symmetry line ($y/W = 0$) of the bottom trailing edge of the base of the body, Fig. 1.

2.2 Numerical Setup

2.2.1 Domain and Boundary Conditions. It has been seen in several studies that the flow around the rear of the Ahmed body with 25 deg slant angle is insensitive to the Reynolds number [8,9,27]. To be able to directly compare the simulation results to previous high-resolution PIV measurements [8,30], the same Reynolds number as in the measurements is used for the simulations. The Reynolds number, $Re_L = 9.34 \times 10^4$, is based on the length of the body.

To achieve similar flow conditions as in the PIV measurements [8,30] the full test-section is modeled, Fig. 1. The test-section floor reach $4.2H$ upstream of the body and has a 4:1 elliptical leading edge. In the measurements, the flow is also allowed to pass below the splitter plate through an empty tunnel section [8,30]. To ensure small and negligible effects from the inlet boundary condition, the inlet is positioned an additional $8.3H$ upstream of the leading edge of the test-section floor. The bottom part of the domain upstream of the elliptical leading edge is modeled with symmetry condition, to replicate the freestream upstream the test-section. The outlet of the domain is positioned $20.8H$ downstream of the body and modeled with zero-static pressure. The freestream entering the domain is modeled with a uniform velocity profile. The width and height of the tunnel was both $8.3H$, resulting in a solid blockage of less than 2% as in the measurements [8,30]. In Refs. [8] and [30] a turbulent intensity of less than 0.5% was measured together with a nonuniformity of $\pm 1\%$ for the velocity profile at the test-section. To ensure no or

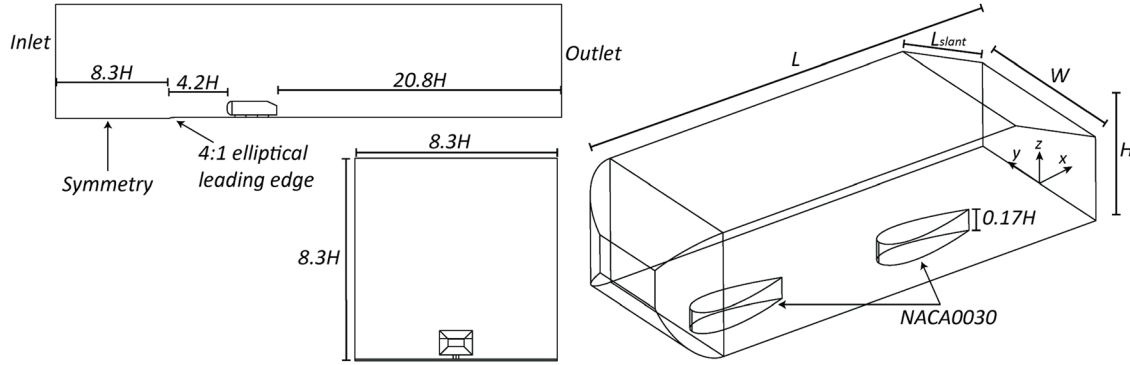


Fig. 1 Drawing of the Ahmed body in the simulated domain. The domain is modeled after the water tunnel used in the PIV measurements.

minor effects of the inflow conditions, two different turbulence intensities, 1 and 5%, were evaluated at the inlet (generated with a spectral synthesizer), which resulted in only very minor differences for the parameters presented in this study. A turbulence intensity of 1% at the inlet is therefore used, resulting in a turbulence intensity of less than 0.5% in the test-section, as seen in the measurements. The surfaces of the model and walls of the water tunnel are modeled with no-slip condition.

2.2.2 Large Eddy Simulations Governing Equations. The governing LES equations are the incompressible Navier–Stokes and continuity equations filtered with the implicit spatial filter of characteristic width Δ (Eqs. (1) and (2))

$$\frac{\partial \bar{u}_i}{\partial t} + \frac{\partial \bar{u}_i \bar{u}_j}{\partial x_j} = -\frac{1}{\rho} \frac{\partial \bar{p}}{\partial x_i} + \frac{\partial}{\partial x_j} \left(\nu \frac{\partial \bar{u}_i}{\partial x_j} \right) + \frac{1}{\rho} \frac{\partial \tau_{ij}}{\partial x_j} \quad (1)$$

$$\frac{\partial \bar{u}_i}{\partial x_i} = 0 \quad (2)$$

Here, ν , \bar{u}_i , and \bar{p} are the kinematic viscosity and the filtered variables for the resolved velocity and pressure, respectively. τ_{ij} is the SGS turbulent stress defined in the following equation:

$$\tau_{ij} = \bar{u}_i \bar{u}_j - \bar{u}_i \bar{u}_j \quad (3)$$

The SGS turbulent stresses are unknown and need closure, and there exist several ways to do that. In this study, three frequently used SGS models were investigated, the SM model, the DSM model and the WALE model. All these three models are based on the concept of isotropic eddy-viscosity (in the following equation) for determining the SGS turbulent stress:

$$\tau_{ij} - \frac{1}{3} \tau_{kk} \delta_{ij} = -2\mu_{\text{SGS}} \bar{S}_{ij} \quad (4)$$

Here, μ_{SGS} is the SGS eddy-viscosity, defined by each SGS-model, and \bar{S}_{ij} is the resolved rate-of-strain tensor (in the following equation):

$$\bar{S}_{ij} = \frac{1}{2} \left(\frac{\partial \bar{u}_i}{\partial x_j} + \frac{\partial \bar{u}_j}{\partial x_i} \right) \quad (5)$$

2.2.2.1 Smagorinsky-Lilly model. The SM model was first proposed by Smagorinsky [33] where the kinematic eddy-viscosity is $\mu_{\text{SGS}} = \nu_{\text{SGS}}/\rho$ and is modeled as

$$\nu_{\text{SGS,SM}} = L_s^2 |\bar{S}| \quad (6)$$

Here, L_s is the mixing length for the sub-grid scale and $|\bar{S}| = (2\bar{S}_{ij}\bar{S}_{ij})^{1/2}$. The mixing length, L_s , for the sub-grid scales is defines as

$$L_s = \min(\kappa d, C_s \Delta) \quad (7)$$

where κ is the von Kármán constant, d is the distance to the closest wall, C_s is the Smagorinsky model constant and Δ the grid-filter length. The Smagorinsky model constant, C_s , is in this study equal to 0.1, this value is commonly used as default value in many commercial codes and has also been used in many studies of flow around bluff bodies [23,27]. The grid-filter length, Δ , is computed from the cube root of the volume of each cell, $\Delta = V^{1/3}$.

Since this model does not provide zero eddy-viscosity in laminar flow the model needs a wall-damping function for better near-wall flow behavior. This is achieved by ensuring that the mixing length goes to zero at the wall (Eq. (7)), which gives the same behavior as for the eddy-viscosity.

2.2.2.2 Dynamic Smagorinsky-Lilly model. The DSM model is based on the SM model but with modification of the Smagorinsky model constant, C_s [34]. Instead of using a constant value for C_s it is dynamically computed during the LES and uses information from the smaller scales of the resolved field, resulting in C_{ds} . To separate the smaller scales from the resolved field the DSM model use of a test-filter, $\tilde{\Delta}$. The test-filter is in this study twice the size of the grid filter-length, Δ [34]. This test-filter is used on the governing Navier–Stokes and continuity equations, resulting in a subtest-scale stress defined as

$$T_{ij} = \widetilde{\bar{u}_i \bar{u}_j} - \widetilde{\bar{u}_i} \widetilde{\bar{u}_j} \quad (8)$$

where “ \sim ” denotes the test-filtered variables. In Ref. [34] it can be seen that τ_{ij} and T_{ij} are related to each other and can be used to determine the local value of the dynamic Smagorinsky constant (in the following equation):

$$T_{ij} - \tilde{\tau}_{ij} = L_{ij} \quad (9)$$

Here, L_{ij} is the Leonard stresses, which can be interpreted as the stress associated with the smaller resolved scales between the test-filter, $\tilde{\Delta}$, and the grid-filter, Δ . From this an ad hoc solution [34] of the dynamic Smagorinsky model constant, C_{ds} , can be defined (Eq. (10)) as

$$C_{ds} = \left(\frac{L_{ij} M_{ij}}{M_{ij} M_{ij}} \right)^{1/2} \quad (10)$$

where M_{ij} is defines as

$$M_{ij} = -2 \left(\tilde{\Delta}^2 |\tilde{S}| \tilde{S}_{ij} - \tilde{\Delta}^2 |\tilde{S}| \tilde{S}_{ij} \right) \quad (11)$$

This makes the dynamic model constant, C_{ds} , vary in time and space over a fairly wide range. To avoid numerical instabilities the range is limited between 0 and 0.23, [33,35], however, in this

study C_{ds} never reached the maximum limit. The time-averaged distribution of the C_{ds} variable can be seen in Fig. 1 available in the [Supplemental Materials](#) on the ASME Digital Collection. The effect of the dynamic Smagorinsky model constant makes the model able to have a correct near-wall behavior as the eddy-viscosity automatically go to zero in laminar flows [34,35]. Further details about the model and its implementation in ANSYS FLUENT can be found in Refs. [34] and [35].

2.2.2.3 Wall-adopting local eddy-viscosity model. Another approach to take care of the near-wall behavior is the one used in the WALE SGS model [36]. For WALE the kinematic eddy-viscosity is formulated as

$$\nu_{SGSWALE} = L_s^2 \frac{(S_{ij}^d S_{ij}^d)^{3/2}}{(\bar{S}_{ij} \bar{S}_{ij})^{5/2} + (S_{ij}^d S_{ij}^d)^{5/4}} \quad (12)$$

Here, S_{ij}^d is the traceless symmetric part of the square of the velocity gradient tensor and can be rewritten as a function of filtered the strain-rate, \bar{S}_{ij} , and vorticity, $\bar{\Omega}_{ij}$ (in the following equation):

$$S_{ij}^d = \bar{S}_{ik} \bar{S}_{kj} + \bar{\Omega}_{ik} \bar{\Omega}_{kj} - \frac{1}{3} \delta_{ij} (\bar{S}_{mn} \bar{S}_{mn} - \bar{\Omega}_{mn} \bar{\Omega}_{mn}) \quad (13)$$

L_s is also here the mixing length of the sub-grid scales and defined similarly as for the SM model (Eq. (7)) but with the WALE constant (Eq. (14)). The WALE model constant, C_w , is set to 0.325 in this study, as it seen to be superior for the used solver [37].

$$L_s = \min(\kappa d, C_w \Delta) \quad (14)$$

WALE will also, similar to DSM, provide zero eddy-viscosity for laminar flow. Due to the formulation of the eddy-viscosity it provides an automatic damping function near the wall, and therefore do not need an extra wall-damping function.

2.2.2.4 Near-wall treatment. All the meshes used in this study are fine enough to resolve the laminar sublayer on all no-slip surfaces. Therefore, the wall shear stress is obtained from the laminar stress-strain relationship (in the following equation):

$$\bar{u}^+ = n^+ \quad (15)$$

Here, \bar{u}^+ and n^+ are the nondimensional velocity and normal wall distance, respectively.

2.2.3 Numerical Method. All the simulations are performed with the commercially available cell-centered finite volume solver ANSYS FLUENT 15.0. The pressure based solver is used together with the semi-implicit method for pressure linked equations-consistent pressure-velocity coupling scheme, which is an improved version of the basic SIMPLE algorithm and as a result lead to faster convergence [38]. The spatial discretization of the convective terms in the momentum equations are calculated by use of the bounded central differencing scheme, which enables low numerical diffusion by use of the central differencing scheme, but still ensures stability by blending first and second-order upwind scheme when needed. It is based on the normalized variable diagram [39,40] and the upwind schemes are only used when a convection boundedness criterion is violated. The central differencing scheme is used for the spatial discretization of the diffusion terms. The spatial discretization for the gradients are solved by using the least squares cell based method, which maintain second-order accuracy to a low cost, while the pressure is solved by use of the central differencing scheme.

2.2.4 Temporal and Spatial Resolution. For the transient formulation, the second-order implicit iterative time-advancement is used, with three inner loop iterations for every time-step. This

ensured that the instantaneous solution was converged for the scaled (with the flowrate through the domain) residuals below 10^{-5} for the continuity and momentum equations, at every time-step. These solver settings are maintained during the whole investigation.

The time-step sizes ($\Delta t U_\infty / L$) are 6.4×10^{-4} and 3×10^{-4} for the baseline and fine mesh, respectively. This ensured that the Courant-Friedrichs-Lewy number was below unity in all the cells for the whole solution. The simulations performed on the baseline mesh is started from a previously run steady-state simulation with the $k-\omega$ shear stress transport turbulence model [41].

A larger time-step size of 1.2×10^{-3} is used in the beginning of the simulation for 20 convective flow units ($t = U_\infty / L$) to minimize possible initial effects. The simulation then run for another 20 convective flow units before time averaging of the filtered variables are done for 100 convective flow units. The fine mesh is initialized from the baseline solution, and then run for 20 convective flow units with the small time-step size before time averaging of the filtered variables for 80 convective flow units. This resulted in well-averaged flow fields with less than 1% of fluctuations of the time-averaged forces over the last 20 convective flow units, see Fig. 2 available in the [Supplemental Materials](#) on the ASME Digital Collection.

The meshes are created in the commercially available grid generator software ANSYS ICEM CFD 15.0, and consist of hexahedral elements. Two different grid levels are investigated, in order to check the grid sensitivity of the results. The baseline and the fine meshes consist of 33.79 and 55.27 million cells, respectively. For the mesh sensitivity analysis, the drag and lift coefficients (Eqs. (16) and (17)) and vortex center locations are compared between the coarse and fine mesh for the DSM SGS model.

$$C_D = \frac{F_x}{0.5 \rho U_\infty^2 A} \quad (16)$$

$$C_L = \frac{F_z}{0.5 \rho U_\infty^2 A} \quad (17)$$

Here, F_x is the drag force, F_z the lift force, ρ the density of the fluid, U_∞^2 the freestream velocity in test-section and A the projected frontal area of the Ahmed body (neglecting the stilts). No significant differences in drag and lift or its distribution are observed between the meshes, as only small differences can be seen (Table 1). A difference less than $0.065H$ of the C-pillar vortex z -position around $x/L = 0.3$ is seen between the meshes. Due to the small differences, the baseline mesh is deemed fine enough, and thereby used in this study.

The meshes consist of rectangular blocks while the model is enclosed in an O-grid for more efficient cell distribution. The first node is positioned $1.38 \times 10^{-3}H$ from the body surfaces and the ground of the test-section in order to ensure a nondimensional wall unit of $n^+ < 1$, where $n^+ = \Delta n \langle u_\tau \rangle_t / \nu$. Here, Δn is the first cell thickness, $\langle u_\tau \rangle_t$ the time-averaged friction velocity and ν the kinematic viscosity of the fluid. For the tunnel walls and ceiling, the first node is positioned at $2.74 \times 10^{-3}H$ resulting in $n^+ < 3$. This is done to obtain a proper boundary layer build up inside the test-section and thereby similar blockage effects as in the experiments [8,30].

To ensure fine enough resolution in the stream wise and the span wise direction, a maximum cell size of 14 times the wall normal distance is used at the walls of the model for the baseline mesh. This corresponds to 100 nodes covering the body in the y -direction (width of the model), 266 in the x -direction (length of the body) and 90 in the z -direction (height of the body) plus an additional 44 nodes covering the stilts. This resulted in a mesh resolution where the majority of the cells (99.96%) at the walls of the body reached values of $s^+ < 20$ and $l^+ < 40$ for the spanwise and streamwise nondimensional wall units, respectively. Here, $l^+ = \Delta l \langle u_\tau \rangle_t / \nu$ and $s^+ = \Delta s \langle u_\tau \rangle_t / \nu$, where Δl and Δs are the spanwise and streamwise cell sizes, respectively, which follows

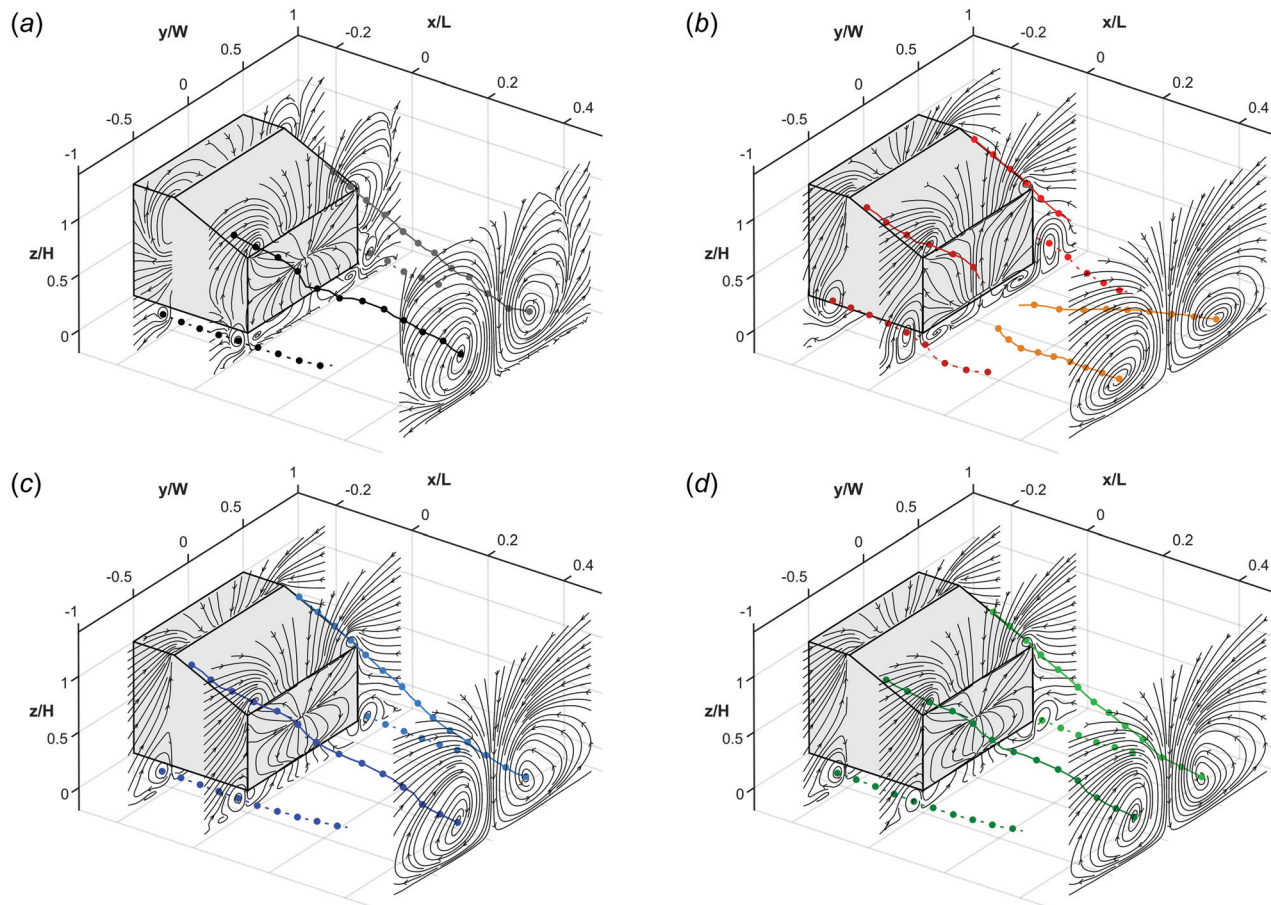


Fig. 2 Time-averaged two-dimensional (2D) streamlines in three yz -planes located at $x/L = [-0.2, 0.0, 0.5]$ for the PIV measurement (a), SM (b), DSM (c) and WALE (d). Solid lines and dotted lines represent the vortex center of the C-pillar and corner vortices, respectively. The orange dotted lines in (b) represent the vortex center for the far wake of the SM SGS model. Only every second point for the vortex centers are shown for clarity.

Table 1 Drag and lift coefficients for the full body and sections of it for the two investigated meshes

Mesh	$C_{D,Total}$	$C_{D,Front}$	$C_{D,Slant}$	$C_{D,Base}$	$C_{L,Total}$	$C_{L,Slant}$
Coarse	0.422	0.012	0.139	0.094	0.242	0.297
Fine	0.426	0.012	0.140	0.096	0.235	0.295

the recommendation for turbulent channel flow [42]. A growth ratio smaller than or equal to 1.15 is set for the mesh in the vicinity of the body while a growth ratio of up to 1.3 is set further away from the body and tunnel walls, where only undisturbed freestream flow is expected. The same resolution but with fewer cells covering the width of the body is used for the 80% width body. The mesh cell quality is kept above 0.35 (where a value of 1 represent a perfect hexahedral cube) for the normalized Jacobian determinant, max orthogls and warp.

In earlier studies, there have been divided views on the need for the mesh resolution upstream the slant. Krajnovic and Davidson [27] assumed that the upstream flow had a minor impact on the flow downstream the slant, while Serre et al. [22] and Ashton and Revell [21] emphasized the need to accurately capture the fluctuations upstream of the slant. This is due to its large effect on the reattachment on the slant. In this study, the baseline mesh is fine enough to capture the fluctuating flow caused by the separation at the front of the body. Due to the low Reynolds number, a larger separation at the front is expected and thereby make it even more

important to capture the fluctuations upstream the slant. Mesh refinement is done at the rear and downstream the body, to capture the vortical structures in the wake.

The baseline interior mesh resolution is analyzed in detail for the DSM SGS model, and assumed to be of enough resolution for the other SGS models. The amount of resolved turbulent kinetic energy (TKE) is calculated in all the cells that had more than 10% turbulent kinetic energy of the maximum value, in the following equation:

$$M(x, t) = \frac{k_{tot}(x, t) - k_{sgs}(x, t)}{k_{tot}(x, t)} \quad (18)$$

Here, $M(x, t)$ is evaluated in each cell and is the percentage amount of resolved turbulent kinetic energy and $k_{tot}(x, t)$ the total turbulent kinetic energy. $k_{tot}(x, t)$ is the summation of the SGS modeled, $k_{sgs}(x, t)$, TKE and resolved TKE, $k_{res}(x, t)$. The modeled TKE can be estimated for the SM and DSM SGS models by

$$k_{sgs}(x, t) = \frac{\nu_t(x, t)^2}{(\Delta(x, t) C_{ds}(x, t))^2} \quad (19)$$

where ν_t is the kinematic turbulent viscosity, Δ the filter width and C_{ds} is the dynamic Smagorinsky model constant. It is seen that the majority of the cells resolve more than 80% of the total turbulent kinetic energy, which is deemed enough [43].

The eddy-viscosity ratio, ν_t/ν , was also monitored to provide an indication of the ratio between the modeled and resolved

contributions to the dissipation [44]. It reached a maximum of 2.3 near the body, while reaching a maximum of 8.3 in the whole domain. Ideally this should be as close as possible to unity, and at least stay below 10 [44].

The normalized two-point correlation (Eq. (20)) is also computed in three representative regions (top of the body, slant and downstream of the front stilt), as it has been shown to be more reliable than the other measures for estimating mesh resolution [45,46].

$$B_{11}^{\text{norm}}(x_1^A, \hat{x}_1) = \frac{1}{v_{1,\text{rms}}(x_1^A) v_{1,\text{rms}}(x_1^A + \hat{x}_1)} \overline{v_1'(x_1^A) v_1'(x_1^A + \hat{x}_1)} \quad (20)$$

Here, x_1^A denotes the starting point, \hat{x}_1 the distance from the starting point A, v_1 the velocity component and v_1' the fluctuating part of the velocity component.

For the separated flow at the top part of the front of the body, a signal correlation of 0.2 or higher is observed for seven cells, while more than 14 cells cover it downstream the front stilt and at the slant. This is well above the recommendations of at least eight cells [45,46] for the slant and front stilt, while just below for the top part of the front of the body. For sampling locations and correlation signal, please see Fig. 3 available in the [Supplemental Materials](#) on the ASME Digital Collection.

From the mesh sensitivity analysis and mesh resolution metrics, only small differences to the result occur when refining the mesh. The baseline mesh follows the resolution recommendations presented in Refs. [21] and [42–46].

2.3 Particle Image Velocimetry. Particle image velocimetry was used to measure the velocity field in the wake of the Ahmed body. The ground plane and the body were placed upside down in the water channel at Fluids Laboratory for Aeronautical and Industrial Research (FLAIR) at Monash University, Australia. The water channel is a free-surface, closed circuit channel with a cross section 600 mm wide \times 800 mm high and is 4000 mm long. With a freestream velocity of 0.365 m/s, the Reynolds number was 9.34×10^4 , based on the length of the Ahmed body.

The flow was seeded with spherical particles and illuminated with a 532 nm laser. Images were acquired with a PCO 4000 (10.7 Mpx) charge-coupled device camera or a PCO Dimax S4 (4.1 Mpx) CMOS camera for the planes. The image pairs were analyzed using in-house cross-correlation software [47] with a window size of 32×32 pixels and an overlap of 75%. For complete details about the experimental setup and PIV acquisition, the reader is referred to [8,30].

2.4 Post-Processing. For fair comparison, the CFD results which are compared to the PIV measurements were exported as a stack of 2D grids for the cross-stream (yz) and the streamwise (xz) planes, with a resolution of $0.006W$ and $0.003H$, respectively. The same resolution as used for the PIV measurements in Refs. [8] and [30].

The vortex center was calculated by use of the scalar function, Γ_1 , presented in Ref. [48], Eq. (21). Γ_1 is a scalar related to the rotation of the fluid in a 2D region of interest around each point. It is determined by the direction of each velocity vector in the region and generates a local maximum in the center of a vortex

$$\Gamma_1(P) = \frac{1}{N} \sum_s \sin(\theta_M) \quad (21)$$

Here, N is the number of points M inside S and θ_M the angle between the velocity vector at M and the radius vector between P and M . From a sensitivity analysis of the needed points in M , it

was determined that a 7×7 points was sufficient for finding the vortex centers, even close to the boundaries. Γ_1 values over 0.7 together with a local maximum within M was used for establishing the center of the vortex.

3 Results and Discussion

The Ahmed body was originally developed for studying the separation over the slant and the effect of the C-pillar vortices. Even for a greatly reduced Reynolds number (compared to original study by Ahmed et al. [2]) these structures still dominate the flow at the rear of the body [6,8–10].

In Fig. 2, the time-averaged vortex centers and 2D streamlines in three yz -planes, $x/L = [-0.2, 0.0, 0.5]$, can be seen for PIV and the three investigated SGS models. The C-pillar vortices can clearly be seen, as the flow rolls up over the C-pillar and causing strong vortices that are present several body lengths downstream.

Strong similarities are noted between the PIV measurements, DSM and WALE models, as the C-pillar and corner vortices follow similar behavior and paths. However, the SM model predicts a completely different behavior for the C-pillar vortices, downstream of the body. For the SM SGS model the C-pillar vortices break up around $x/L = 0.125$, while for the PIV, DSM and WALE SGS models they are present several body lengths downstream of the body. In all cases, the C-pillar vortices are present from the beginning of the slant, but are detected slightly downstream due to the used Γ_1 threshold value and PIV resolution.

Further downstream the wake, at $x/L = 0.5$, similar flow behavior between all the SGS models and PIV can be seen, as the flow is dominated by two counter-rotating vortices. It should be noted, however, that the vortices causing a seemingly similar behavior for the SM model is in fact the effect of two counter-rotating vortices originating from an interaction of the C-pillar and corner vortices. Due to this, the far wake has similar behavior between all three SGS model and the PIV measurements, even though the SM SGS model captures a completely different near wake behavior.

Close to the vertical base of the body, a similar behavior for the near-wall flow are seen for the DSM and WALE SGS models, when compared with the PIV measurements. Both these SGS models are able to capture the saddle point at the middle of the vertical base of the body, indicating the presence of two spanwise vortices in the near wake. For the SM SGS model the saddle point exist near the bottom edge of the vertical base with the near-wall flow mainly in the z -direction, indicating a single large spanwise vortex in the near wake region.

A small negative bifurcation is noted on the top and bottom part of the base in Ref. [8]. The top bifurcation is caused by the flow reattaching on the slant, causing separation over the top part of the base. The bottom bifurcation is caused by the flow under the body separating at the bottom edge of the base. All three SGS models are able to capture both the bifurcations (see Fig. 4 available in the [Supplemental Materials](#) on the ASME Digital Collection), but not to the same extent as seen in Ref. [8]. The SM SGS model is only able to capture the small negative bifurcation on the top part of the base, while the DSM and WALE SGS models are only able to capture the bottom negative bifurcation. This is mainly due to the different spanwise vortical structures in the wake.

The flow under the body is accelerated as an effect of the cross-sectional area underneath the body. Due to the stationary ground, a boundary layer exist on the test-section floor and on the body, causing the flow outward to the lateral sides of the body to satisfy continuity. This forms the longitudinal corner vortices, which travels along the bottom side of the body, Fig. 2.

In Fig. 3, the position of the C-pillar and corner vortices are compared for the PIV and the three investigated SGS models. Excellent agreement with the PIV measurements can be seen for the DSM and WALE SGS models. Due to the different near wake structure for the SM SGS model, the C-pillar vortices are, as described earlier, not present after $x/L = 0.125$. For the y -position

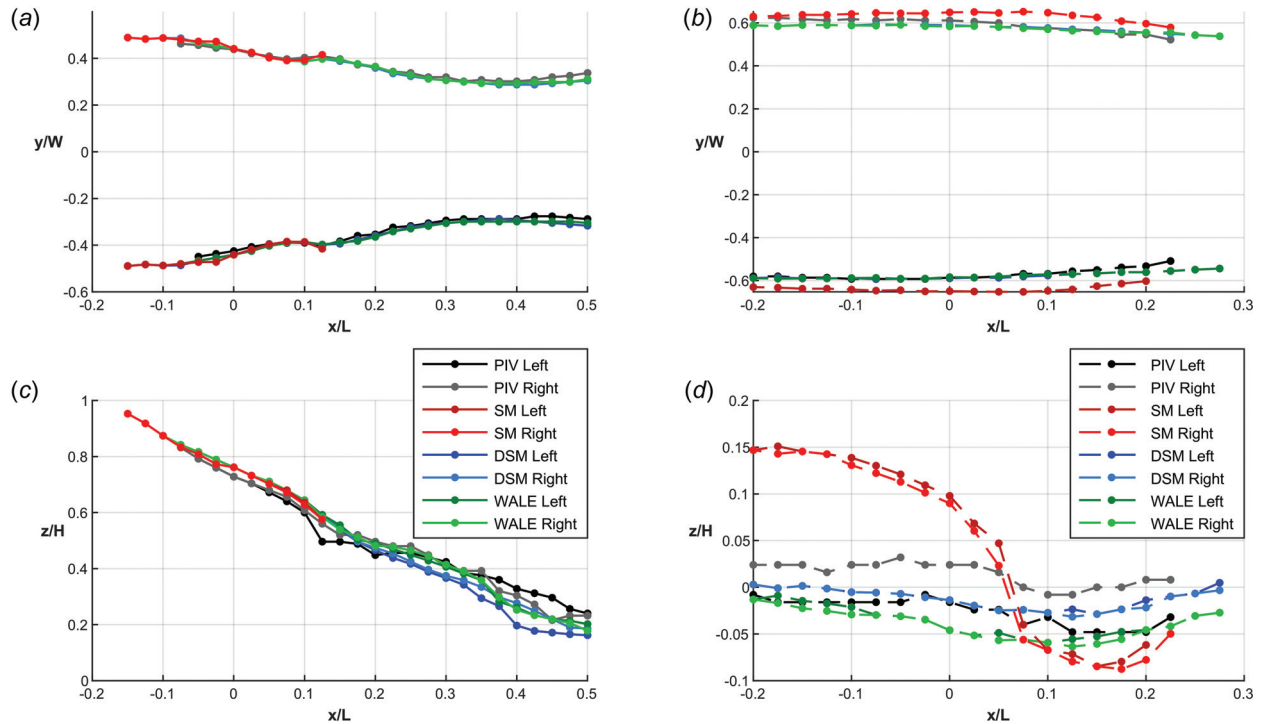


Fig. 3 Comparison of the C-pillar vortex x and y location (a) and x and z location (c), for the PIV measurements and the three investigated SGS models. In (b) and (d), the location of the corner vortices are compared for the PIV measurement and the SGS models.

of the C-pillar vortices, a clear similarity can be seen between the PIV and the DSM and WALE SGS models. A slight difference for the y -position can be seen downstream $x/L = 0.4$, but is mainly an effect of the asymmetry in the PIV measurement. Asymmetrical effects up to $y/W = 0.0492$ and $z/H = 0.080$ can be seen for the C-pillar and corner vortices in the PIV measurements.

In Thacker et al. [7] the behavior of the C-pillar vortices vary linearly in y - and z -position with the x -direction until the end of the body, when the C-pillar vortices are reported to turn downward (z -direction) with an angle change of 14.7 deg. This cannot be seen for either the PIV measurements or the investigated SGS models in this study. This is believed to be due to the much higher Reynolds number used in Ref. [7] ($Re_L = 2.2 \times 10^6$) causing an earlier reattachment on the slant and resulting in lower pressure, which turn the C-pillar vortices toward the $y/W = 0$ plane. This inward movement make the C-pillar vortices more affected by the vortical structures in the wake, and hence less inward movement of the C-pillar vortices is seen in this study.

The reason the corner vortices stop existing after around $x/L = 0.225$ (Fig. 3(d)) is that there is a complex interaction between them and the C-pillar vortices. Both the corner vortex and C-pillar vortex have the same rotation direction, on each side, and hence the top part of the corner vortex and the bottom of the C-pillar vortex have opposite direction causing a decrease in strength of both vortices. When comparing the SGS models with the PIV data for the corner vortex center position, it can clearly be seen that the SM SGS model is not able to capture it accurately. This is caused by the different near wake structure for the SM SGS model. It can also be seen that these vortices are already pushed further away (y -position) from the model, as compared to the other methods. The corner vortices size for the SM SGS model is also larger (Fig. 2) but weaker than seen for the DSM and WALE SGS models, as three times lower Q -criterion is observed in them at $x/L = 0$.

The opposite behavior as seen for the C-pillar vortices can be seen here for the DSM and WALE SGS models. Here, the DSM

SGS model is able to better capture the behavior and location of the corner vortices seen in the PIV measurements. The y -position is almost identical between the SGS models, but for the z -position the DSM SGS model is more aligned with the PIV measurements.

As reported in Ref. [49], the corner vortices kept their initial position in the yz -plane along and behind the body. Here, however, it can be seen that these vortices keep their position in the yz -plane until $x/L = 0.05$, where they tend to move toward the $y/W = 0$ plane and the floor of the test-section.

The main reason for the differences in the results between the investigated SGS models can be connected to the flow beneath the body. In Fig. 4, the skin friction lines and its x -component is seen for the underside of the body. A large region of negative x -skin friction can be seen for the SM SGS model. This cause the flow to reverse in under the body. This reversed flow is a result of the flow separating around 23% of the chord length of the front stilt and that the flow is never able to reattach on either of the front and rear sills. The WALE SGS model separates just slightly later than the SM SGS model, but reattaches at the rear stilt, resulting in less impact on the rear wake of the body. For the DSM SGS model, the flow separates later on the front stilt (around 30% of the chord length) and the wake from the front stilt is kept within the width of the stilts, causing an earlier reattachment on the second stilt.

Stronger outflow (y -direction) below the body can be seen for the SM SGS model, compared to the other two SGS models. This is the reason for the different behavior of the corner vortices. More of the flow is pushed outward from the underside of the body, causing the size of the corner vortices to grow (Fig. 2).

Due to smaller cross-sectional area, the flow accelerate below the body, and a lower static pressure occur and makes this region very sensitive for the downstream flow and the behavior of the wake. The different separation between the SGS-models thereby have a strong impact on the behavior of the flow below and thereby downstream of the front stilt, exposing the strengths and weaknesses of the investigated SGS models. This, also, show the

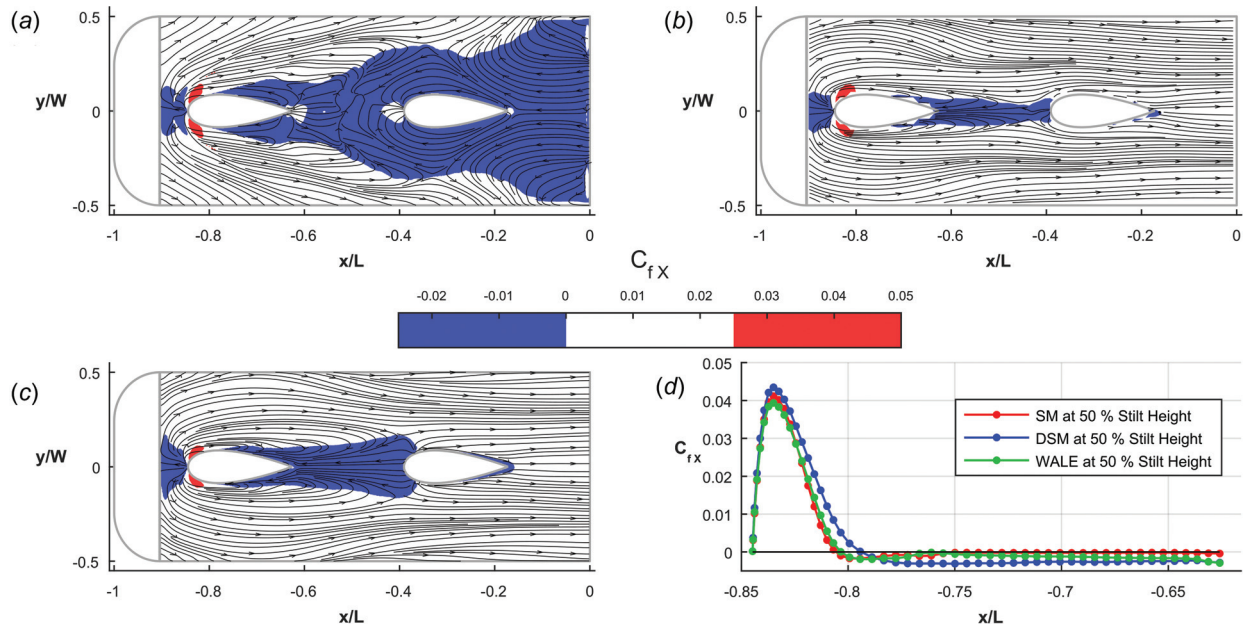


Fig. 4 Time-averaged skin friction lines together with low and high x-skin friction coefficient contour at the bottom side of the body, for the SM (a), DSM (b), and WALE (c). X-skin friction coefficient along the first stilt, at half the stilt height (d).

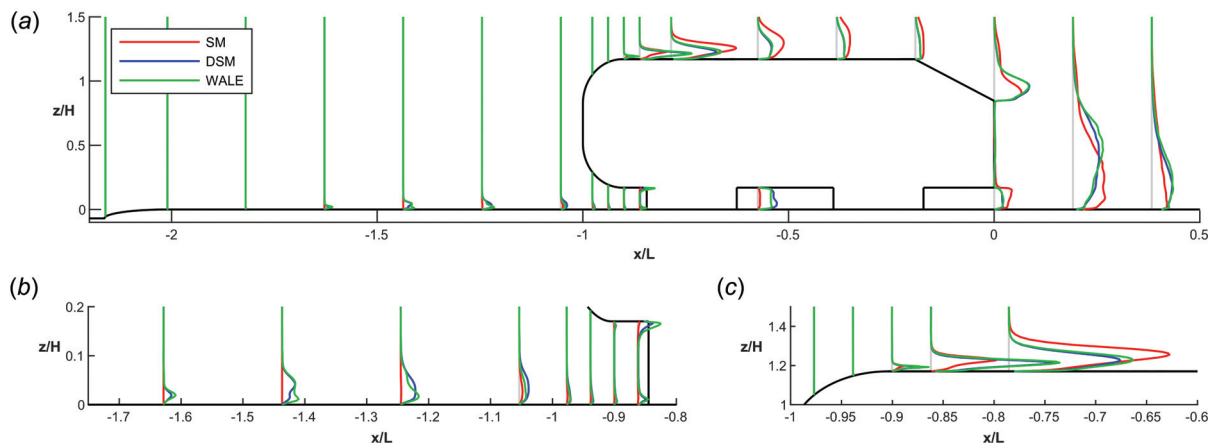


Fig. 5 Time-averaged resolved turbulent kinetic energy lines for the three investigated SGS models in the $y/W=0$ plane. (b) Zoom in on the resolved turbulent kinetic energy upstream the body. (c) Zoom in on the resolved turbulent kinetic energy on the top front part of the body.

geometrical sensitivity of this region, where a small geometrical and/or setup difference may cause severe effects on the downstream flow and behavior of the wake. A setup with different stilt geometry and/or position may therefore be more beneficial to easier replicate studies of this body, especially at lower Reynolds numbers.

Due to the slightly larger separation around the front stilt for the WALE SGS model, compared to the DSM SGS model, it was believed that a narrower body might cause a larger difference or even a larger separation (as seen for the SM SGS model). However, a set of simulations for an 80% width Ahmed body was performed, resulting in the same behavior and differences as seen for the 100% width Ahmed body, for the SM, DSM and WALE SGS models.

The reason for the different separation on the front stilt for the investigated SGS models, is due to the different near-wall flow behavior and the modeling of dissipation for the small structures. In both the DSM and WALE SGS models the near-wall damping is built into the models, resulting in no need for an extra wall-damping function, which is the case for the SM SGS model. This

causes the eddy-viscosity to automatically go toward zero near the wall for the DSM and WALE SGS models, while the SM SGS model need to rely on the von Kármán constant and the distance to the closest wall, d , to reduce the eddy-viscosity. This introduces too much eddy-viscosity near the wall, which dampens the fluctuations and creates a less turbulent boundary layer that separates earlier. For the SM SGS model the eddy-viscosity ratio (ν_{SGS}/ν) reaches a maximum of 1 within the first five cells (in the wall normal direction) between the leading edge and the separation point. This is twice and four times larger than seen for the WALE and DSM SGS models, respectively. This have a significant impact on the instabilities and much less resolved fluctuations occur within this region for the SM SGS model when compared to the DSM and WALE SGS models. Directly upstream of the model, differences between the SGS models for the resolved TKE can be seen near the floor of the test-section, Fig. 5. The SM SGS model resolves less fluctuations, resulting in less resolved TKE upstream the body and the front stilt, as a turbulent boundary layer on the floor of the test-section first occur $0.24L$ upstream the body. This is an effect of more introduced eddy-viscosity for the SM SGS

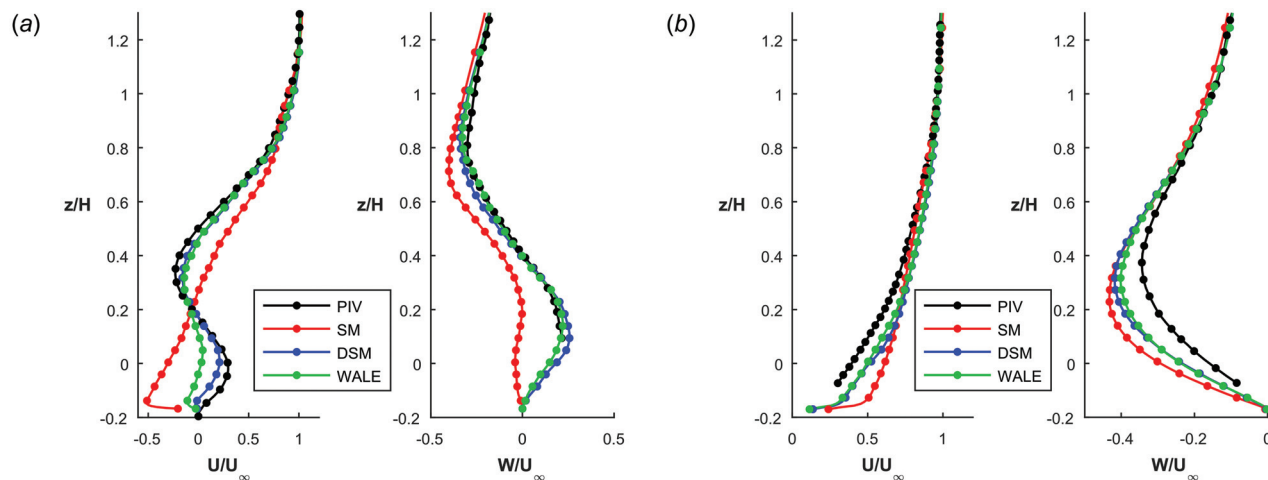


Fig. 6 Comparison of velocity components from both the PIV measurements and the three investigated SGS models, at lines positioned at $x/L = 0.084$ (a) and $x/L = 0.420$ (b). Every fourth and tenth point for the PIV and SGS models, respectively, are shown for clarity.

model, which is introduced directly from the leading edge of the test-section floor. Both the DSM and WALE SGS models also introduce eddy-viscosity in this region, but with slightly less magnitude and starting from around half the distance between the leading edge of the test-section floor and the body, which leads to a turbulent boundary layer starting $0.6L$ upstream the body. For the DSM and WALE SGS models a clear laminar to turbulent transition of the boundary layer on the test-section floor occurs $0.9L$ upstream the body.

The same behavior can be seen for the front top part of the body, where a much larger separation occurs for the SM SGS model, compared to the DSM and WALE SGS models. Here, as well, more eddy-viscosity is introduced near the wall, resulting in less instabilities in the boundary layer and a larger separation, Fig. 5(c). The separation point occurs at the same position (in the $y/W = 0$ plane), $x/L = -0.924$, for all investigated SGS models. Both the DSM and WALE SGS models are here able to capture a turbulent boundary layer before the separation, while it cannot be seen for the SM SGS model. In the same plane, the reattachment point is the same for the DSM and WALE SGS models, $x/L = -0.791$; while for the SM SGS model it is $x/L = -0.716$, which make the separation 56% longer. The separation seen for the DSM and WALE SGS models separation is longest at the $y/W = 0$ position, and behaves similarly in shape and size as seen in water tunnel measurement for a similar Reynolds number [9]. The separation on the top part of the body is larger than the separation on the side of the front for all the investigated SGS model, which is the opposite behavior seen in Ref. [27]. This different separation on the top front part of the body affect the flow behavior just upstream of the slant, where the larger separation for the SM SGS model result in more TKE around the middle section of the body, than for the other two SGS models, Fig. 5(a). This affect the flow over the slant, resulting in an earlier reattachment in the $y/W = 0$ plane, and also move the focus point of the skin friction, caused by the C-pillar vortices, toward the $y/W = 0$ plane, compared to the other two SGS models.

In two vertical lines downstream of the body (located at $x/L = 0.084$ and $x/L = 0.420$) in the $y/W = 0$ plane, the streamwise and vertical velocity components are compared for the three SGS models and PIV measurements, Fig. 6. For the line at $x/L = 0.084$ it can be seen that both the DSM and WALE SGS models are able to capture the same behavior as seen in the PIV measurements. However, the DSM SGS model almost match the PIV measurement perfectly, as only slight differences for the magnitude of the streamwise and vertical velocity can be seen. Especially, below $z/H = 0$ there is differences for the streamwise velocity, which indicates a slightly higher momentum for the flow passing beneath

the body in the PIV measurements. This is important as it imply that the flow is, at least partially, attached to the second stilt. Much higher momentum can be seen for the same location in Ref. [4], as the flow is accelerated in the $y/W = 0$ plane, due to the body is supported by four cylindrical stilts mounted at the outer edge of the body. As the body in this study is supported by two symmetrical airfoils in the $y/W = 0$ plane, the flow tends to be decelerated downstream of the stilts [8]. This also makes the lower part of the wake around the $y/W = 0$ plane very sensitive to the flow around the stilts and may also increase possible asymmetrical effects in the measurements. The line at $x/L = 0.084$ passes right through the spanwise vortical structures in the near wake, which highlights the DSM and WALE SGS models excellent ability to capture a similar wake structure as seen in the PIV measurements.

In Fig. 6(a), the different near wake structure for the SM SGS model is seen: below $z/H = 0.2$ the flow is moving upstream and the streamwise velocity is negative, as an effect of the differently captured underbody flow. The SM SGS model streamwise velocity become similar to the other SGS models only after $z/H = 0.75$, a region dominated by the flow over the central section of the slant. However, for the vertical velocity the SM SGS model differ substantially below $z/H = 0.8$, but follows the same trend as seen for the other SGS models and PIV until $z/H = 0.2$, where a slight negative vertical velocity occurs.

When observing the velocity components at the line positioned further downstream of the body, $x/L = 0.420$, it can be seen that all the SGS models are closer to the PIV measurements (Fig. 6(b)). This is due to the spanwise vortical structures in the wake only reach to around $x/L = 0.25$, resulting in that the velocity at this line mostly is affected by the size of the wake. It can once again be seen that the DSM and WALE SGS models are able to better capture the behavior measured with PIV. For the streamwise flow a higher momentum closer to the floor of the test-section can be seen for the LES compared to the PIV measurements. This can be connected to the higher magnitude of negative vertical velocity in this region for the LES simulations, causing a stronger downwash (z -direction) and higher momentum near the floor of the test-section. Not surprisingly, this downwash is strongest for the SM SGS model, as the flow is drawn down due to the upstream flow beneath the body.

In Fig. 7, the wake in the $y/W = 0$ plane is seen with time-averaged 2D streamlines and spanwise vorticity. In the PIV measurement three spanwise vortices can be seen, one at the top and bottom of the vertical base and one at the ground. The DSM SGS model is the only model able to capture these three vortices in this plane. The WALE SGS model is able to capture the two counter-rotating vortices at the base, but fail to capture the ground vortex

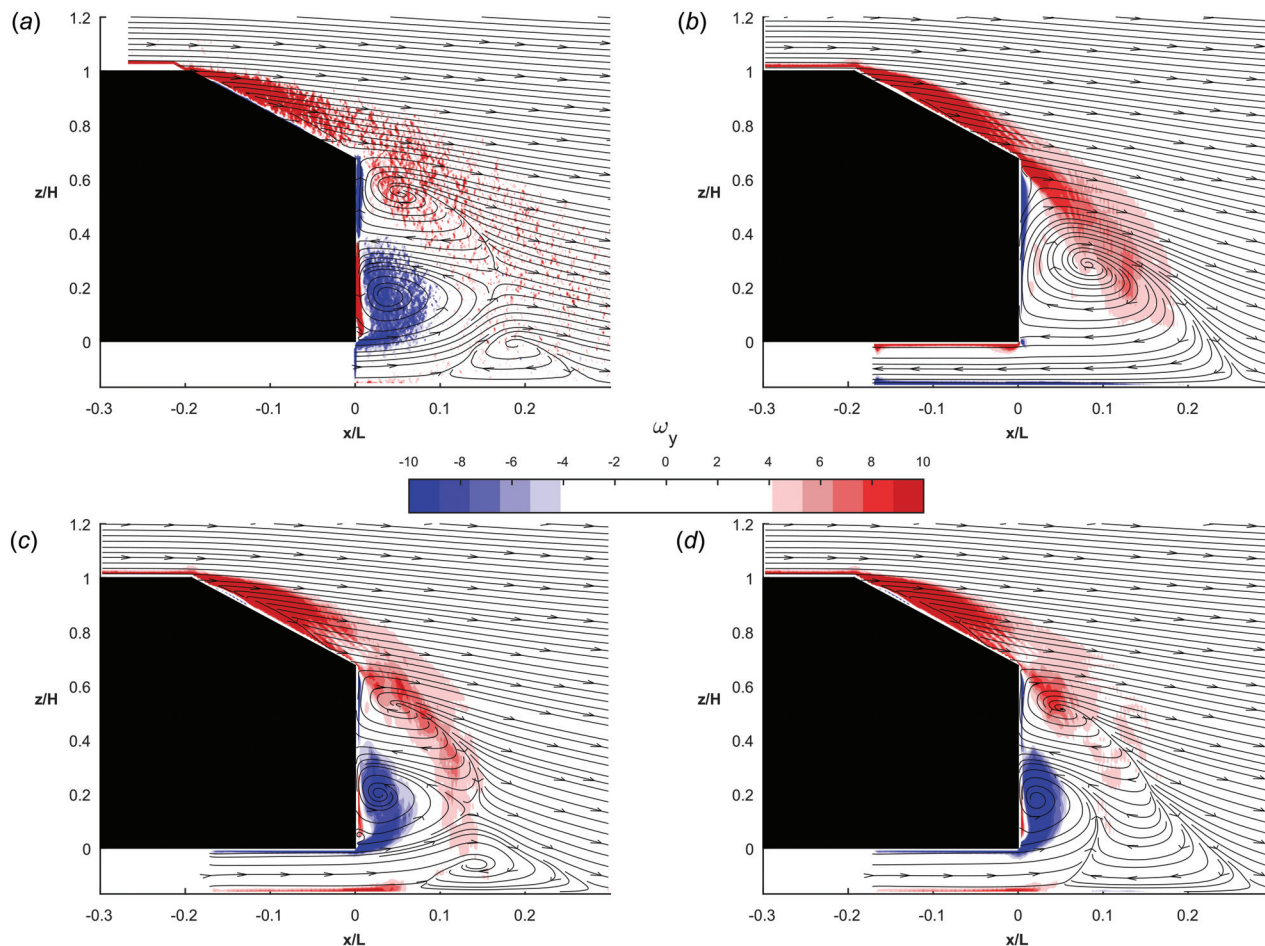


Fig. 7 Time-averaged 2D streamlines and spanwise vorticity in the $y/W=0$ plane for PIV measurement (a), SM model (b), DSM (c), and WALE (d)

at $y/W=0$; only a reversal of the flow exist. The SM SGS model only captures a single clockwise rotating vortex, driven by the reversed flow beneath the body.

All the SGS models captures the large separation over the middle section of the slant, causing a similar behavior of the vorticity (Fig. 7). The SM SGS model predicts more downwash of the vorticity into the wake, as an effect of the single vortex. For the lower base vortex, a region of negative spanwise vorticity is seen in the PIV measurement. Both the DSM and WALE SGS models captures this behavior, where the WALE SGS model tend to concentrate this region more than the DSM SGS model and PIV measurement.

At the $y/W=1/6$ plane, the same trend as for the wake structures seen in the $y/W=0$ plane can be seen (Fig. 8). The SM SGS model still predicts reversed flow beneath the rear of the body, and therefore only captures one large clockwise rotating vortex. For the other two SGS models the behavior is almost similar as in the $y/W=0$ plane (Fig. 7), except now the WALE SGS model overpredicts the clockwise rotating ground vortex at the floor of the test-section, when compared with the PIV measurement. The DSM SGS model is able to more accurately predict the size of this vortex, even though it is slightly larger, than seen in the PIV measurement. This vortex is very dependent of the flow beneath the body and the vertical velocity distribution downstream the body, the latter being dependent of the strength of the two counter-rotating vortices.

All the SGS models are able to predict the positive vorticity from the separated flow over the slant. Note that all the SGS models are able to capture the small zero-vorticity region just above the trailing edge of the slant, as seen in the PIV measurement. The DSM and WALE SGS models capture very similar vorticity

behavior in this plane. However, some differences can be seen for the negative vorticity at the lower counterclockwise rotating vortex, as the WALE SGS model results in a more concentrated region of negative vorticity. For the DSM SGS model a larger region of weaker vorticity is seen, which corresponds well with the PIV measurement.

Also at $y/W=1/3$ the same trend can be seen for the vortical structures in the wake (Fig. 9). The DSM and WALE SGS models are able to capture the two counter-rotating vortices, as also seen in the PIV measurement, while the SM SGS model also here only predicts one large vortex. The DSM SGS model captures a slightly larger bottom vortex, than the WALE SGS model. This behavior is more in line with the PIV measurement. In this plane, no ground vortex at the floor of the test-section exists.

All three SGS models are able to capture similar positive vorticity behavior over the slant and the top part of the near wake. A small region of negative vorticity is seen northeast of the top vortex in the PIV measurement (Fig. 9). This small region is also captured by all SGS-models but shifted slightly to the east. A region of negative vorticity can be seen for the lower part of this vortex. Both the DSM and WALE SGS models captures this. However, the DSM SGS model better captures the strength and shape of it, while not capturing the same negative vorticity magnitude elsewhere in the vicinity, which the WALE SGS model is able to capture.

In the PIV measurement a region of positive vorticity can be seen at $z/H=0.8$ and $x/L=0.1-0.25$, which is an effect of the C-pillar vortex. This effect is not visible in the presented results from the LES simulations, as the magnitude is lower (between 2 and 4 on the colorbar in Fig. 9).

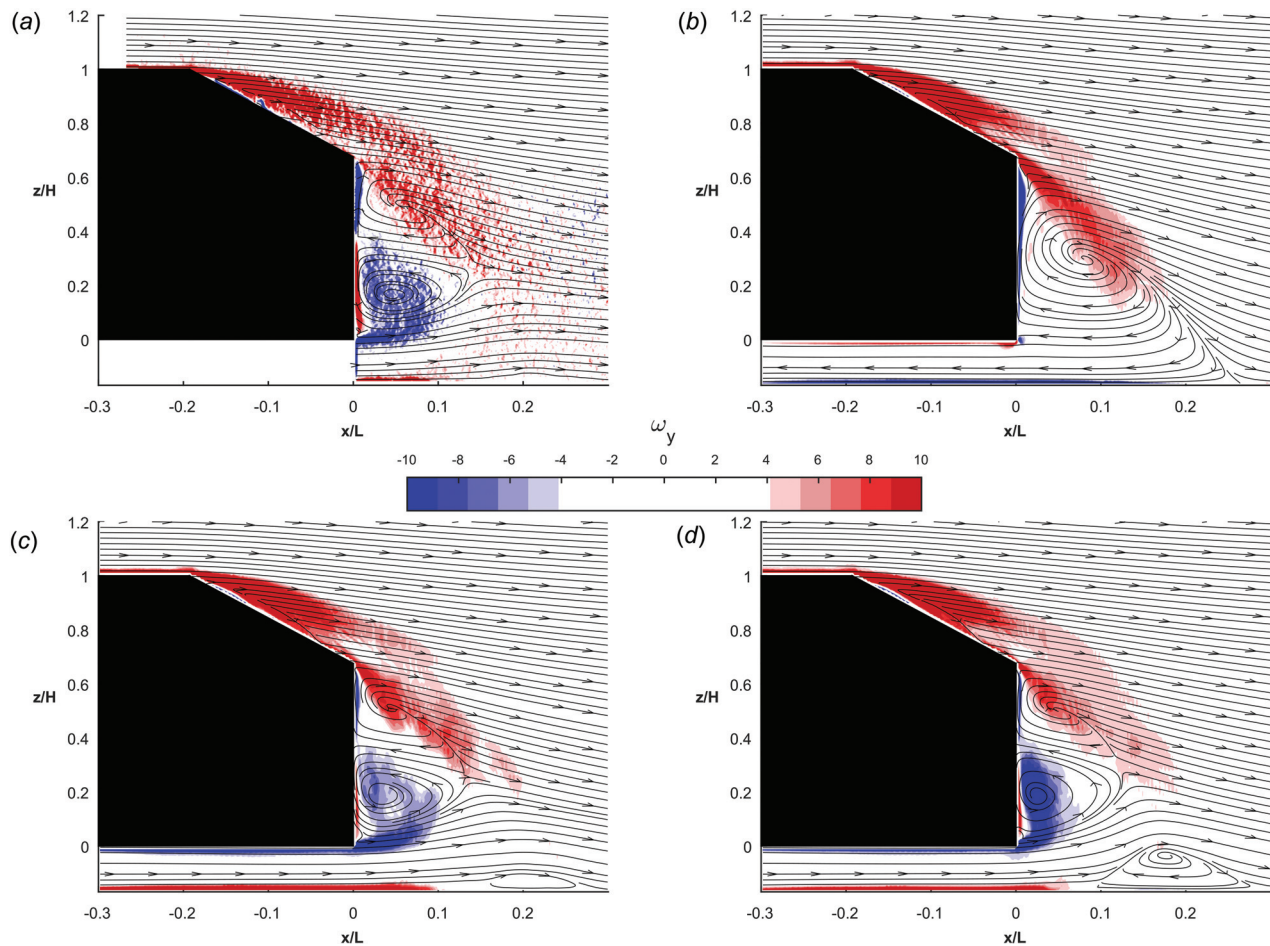


Fig. 8 Time-averaged 2D streamlines and spanwise vorticity in the $y/W = 1/6$ plane for PIV measurement (a), SM model (b), DSM (c), and WALE (d)

The location two counter-rotating spanwise vortices center is seen for the PIV measurement and LES simulations in Fig. 10. Both the DSM and WALE SGS models are able to capture both of the spanwise vortex center locations well when compared with the PIV measurements. For the bottom spanwise vortex slight differences occur for the x -position, except at the widest y -position. Both the spanwise vortex center locations have a parabolic shape behavior for the x -position, which is well captured by both the DSM and WALE SGS models. The SM SGS model captures this behavior, but only for a single spanwise vortex. For the z -position, similar trends are seen with an offset for the top spanwise vortex center location for the DSM and WALE SGS models. The DSM SGS model is able to capture the behavior of the ground vortex, as seen in the PIV measurement, while the WALE SGS model fails near $y/W = 0$. The reason WALE is not able to capture the ground vortex near $y/W = 0$ can be explained by the lower streamwise momentum of the flow downstream of the rear stilt, when compared to the DSM SGS model, Figs. 4 and 6. The lower streamwise momentum cause a stronger upwash of the flow exiting below the body near $y/W = 0$ for the WALE SGS model. This stronger upwash destroys the ground vortex near $y/W = 0$. When moving outboard the vehicle the upwash predicted with WALE move toward the level seen for the DSM SGS model. Supporting this explanation is also that the ground vortex only exist when the stilts are present. A simulation without stilts fitted to the model was done with the DSM SGS model, and resulted in no ground vortex and much less upwash for the flow exiting the below the rear of the body. This explains why no ground vortex is seen for the 25 deg Ahmed body with no or circular stilts [4,6,7,19,22–28].

Even though the SGS modeling only affect the smaller scales, it can be seen to have a significant effect on the overall flow around the Ahmed body. This too much dissipative effect from especially the SM SGS model but also the WALE SGS model have previously also be seen for other cases [32], where flow around bluff bodies has been investigated with LES. As the SM and WALE SGS model is nondynamic they tend to dissipate the largest resolved scales, however, only with a small portion for the WALE SGS model [32]. Use of a dynamic SGS model constant reduces or removes this effect, and make them more suitable for all sort of flows and less sensitive to the mesh resolution. It may be possible to adjust the SGS models constant to better capture the measured flow behavior in a specific case. However, the small extra cost of a dynamic SGS model makes it a much safer choice, especially when considering the already high cost for LES.

4 Conclusion

The effect of the SGS modeling in LES is investigated for three frequently used SGS models, for the flow around the 25 deg Ahmed body. The results are compared to high-resolution PIV measurement done in a water tunnel for a Reynolds number of 9.34×10^4 , based on the length of the body. The water tunnel test-section is modeled in the simulations, to ensure similar conditions as in the experiments. The body is supported by two NACA0030 stilts, instead of the original four circular stilts. This stilt setup is seen to be very sensitive, as small differences in separation around the stilts can cause different wake behavior of the body.

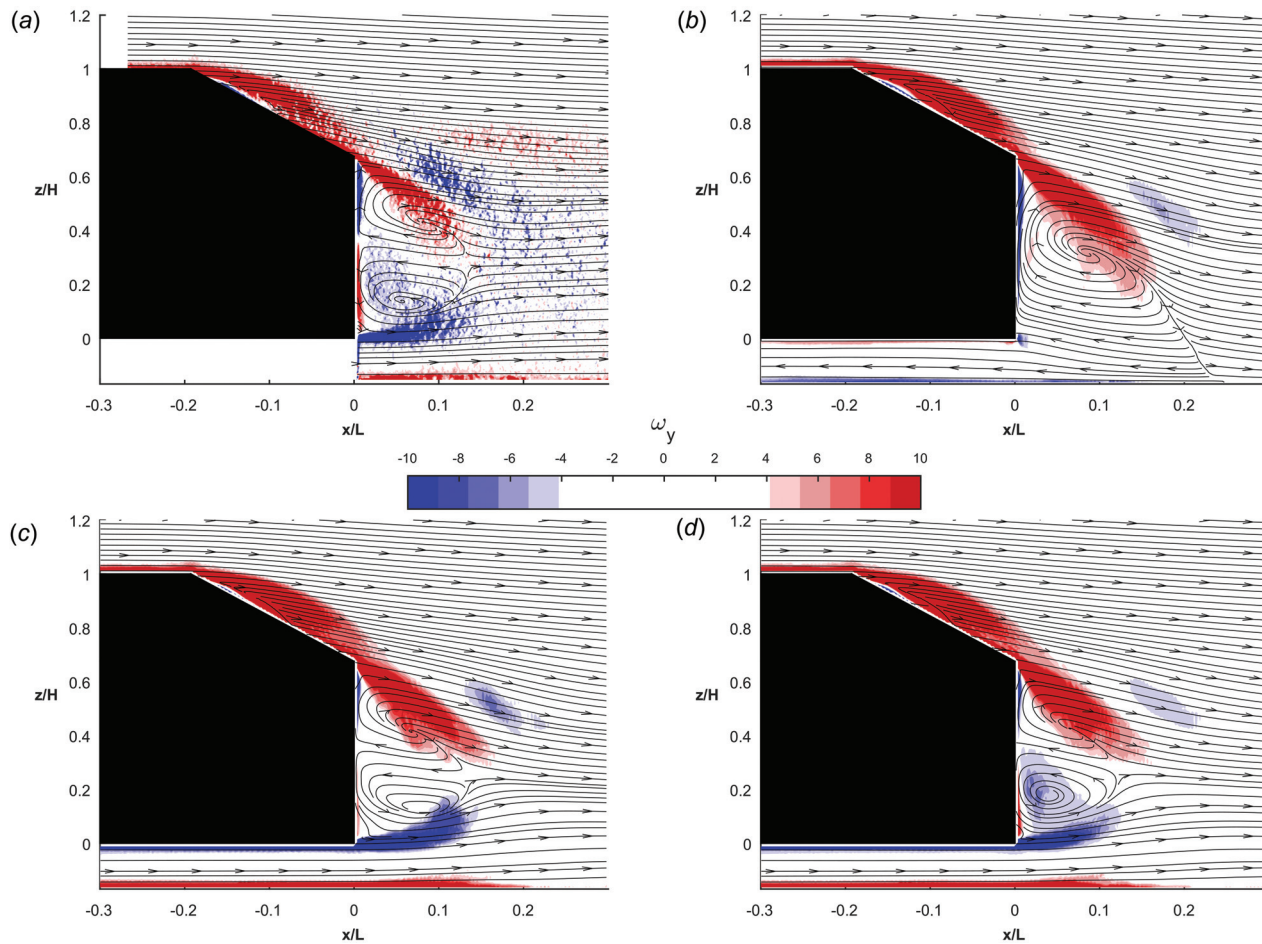


Fig. 9 Time-averaged 2D streamlines and spanwise vorticity in the $y/W = 1/3$ plane for PIV measurement (a), SM model (b), DSM (c), and WALE (d)

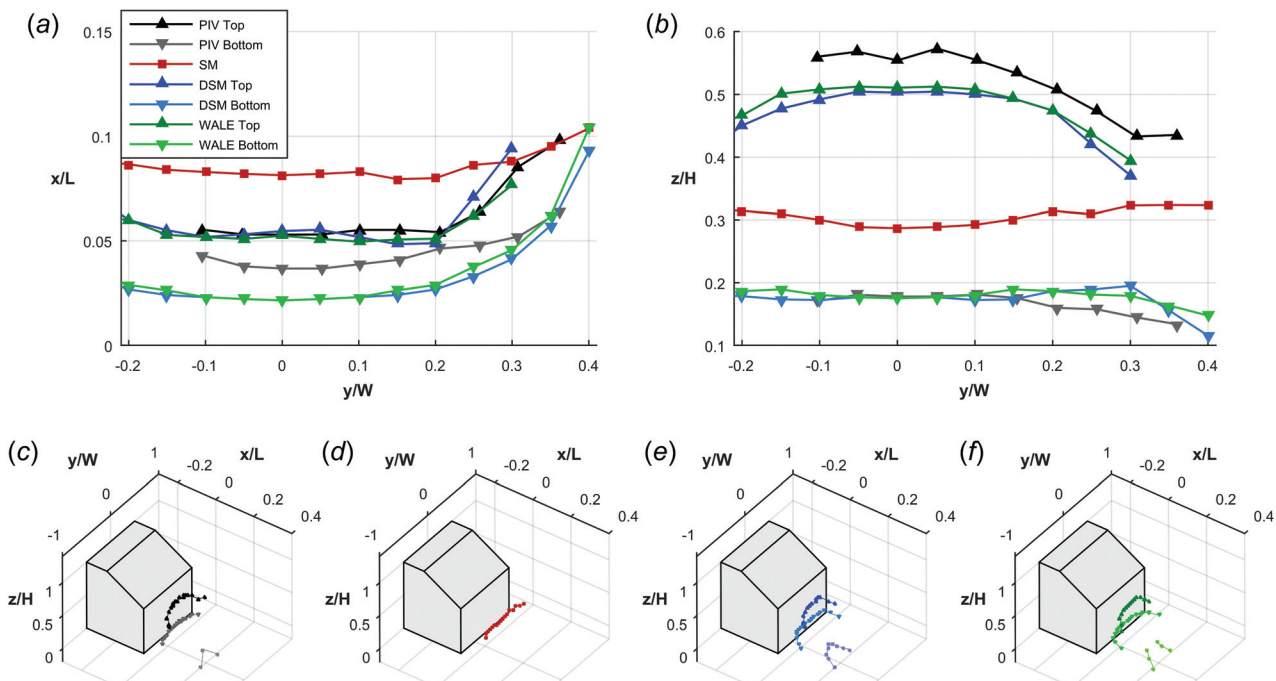


Fig. 10 Spanwise vortex center locations for the investigated SGS models and PIV measurements (a) and (b). The PIV data is taken from Ref. [30], and therefore only exist for $y/W = -0.1$ to 0.37 . 3D views of the spanwise vortices center location (including the ground vortex) for the PIV measurement (c), SM SGS model (d), DSM SGS model (e), and WALE SGS model (f).

Even at the reduced Reynolds number, the original flow characteristics of the Ahmed body is still present, as the flow of the rear part of the body is dominated by the effect of the streamwise and spanwise vortices. The low Reynolds number makes it possible to simulate the flow around the body with wall resolved LES, and still keeping the simulation cost within reasonable limits. The mesh used for the LES in this investigation follow several recommendations of needed mesh resolution, and imply that the mesh resolution is enough to resolve the important turbulent scales.

Special emphasis is put on studying different SGS models' ability to capture the C-pillar and corner vortices of the Ahmed body. The WALE SGS model show best accuracy in capturing the C-pillar vortex center location of the three investigated SGS models, when compared to the PIV measurement. However, it is closely matched with the DSM SGS model, as only slight differences occur further downstream the body. The SM SGS model is only able to capture a part of the C-pillar vortices before the different near wake structure destroy them, as an effect of the different flow beneath the body. The shortcomings of the SM SGS model becomes excessive due to the overpredicted separation around the front NACA0030 stilt. The separation cause a reversed flow beneath the rear part of the body. The DSM and WALE SGS models captures a smaller separation where flow reattaches over the rear stilt. This cause the DSM and WALE SGS models to correlate well with the PIV measurements for all vortical structures. The reason for the significant different flow fields for the SGS models is due to their ability to capture the correct near-wall behavior and their dissipation of the smaller scales. The over-dissipation for the SM SGS model cause the earlier separation on both the front stilt and the front of the body, due to the less instabilities within the boundary layer. The separation on the front of the body also cause more fluctuations in flow passing over the slant and affecting the slant reattachment. The DSM and WALE SGS models do not overestimate the separation on the front part of the body, as an effect of much less dissipation. This cause the DSM and WALE SGS models to be able to capture the spanwise vortices location and the vorticity in the flow field. However, slightly better agreement with the PIV measurement was seen for the DSM SGS model, especially around the $y/W = 0$ plane, which is an effect of the smaller separation on the front stilt causing higher flow momentum in the center beneath the body.

The choice of SGS model which is able to capture the near-wall behavior and small-scale dissipation can be crucial for capturing the correct flow field, especially if the flow is sensitive to low Reynolds number effects and separation over curvatures. This make the DSM and WALE SGS models more robust choices for simulating the flow around the Ahmed body. This motivates the extra cost for a more advanced SGS model, especially as the computational cost for LES already is high. Slightly better agreement with the PIV measurement can be seen for the DSM SGS model, compared to the WALE SGS model. This is an effect of the dynamic constant of the DSM SGS model, which makes it more suitable for a variety of different flows.

Acknowledgment

The simulations were performed on resources provided by the Swedish National Infrastructure for Computing (SNIC) at National Supercomputer Centre (NSC).

References

- [1] Hucho, W.-H., 1998, *Aerodynamics of Road Vehicles*, Society of Automotive Engineers, Warrendale, PA.
- [2] Ahmed, S. R., Ramm, G., and Faltin, G., 1984, "Some Salient Features of the Time-Averaged Ground Vehicle Wake," *SAE Paper No. 840300*.
- [3] Sims-Williams, D. B., and Dominy, R. G., 1998, "Experimental Investigation Into Unsteadiness and Instability in Passenger Car Aerodynamics," *SAE Paper No. 980391*.
- [4] Lienhart, H., and Becker, S., 2003, "Flow and Turbulence Structure in the Wake of a Simplified Car Model," *SAE Paper No. 2003-01-0656*.
- [5] Conan, B., Anthoine, J., and Planquart, P., 2011, "Experimental Aerodynamic Study of a Car-Type Bluff Body," *Exp. Fluids*, **50**(5), pp. 1273–1284.
- [6] Tunay, T., Sahin, B., and Ozbolat, V., 2014, "Effects of Rear Slant Angles on the Flow Characteristics of Ahmed Body," *Exp. Therm. Fluid Sci.*, **57**, pp. 165–176.
- [7] Thacker, A., Aubrun, S., Leroy, A., and Devinant, P., 2012, "Effects of Suppressing the 3D Separation on the Rear Slant on the Flow Structures Around an Ahmed Body," *J. Wind Eng. Ind. Aerodyn.*, **107–108**, pp. 237–243.
- [8] Venning, J., Lo Jacono, D., Burton, D., Thompson, M., and Sheridan, J., 2015, "The Effect of Aspect Ratio on the Wake of the Ahmed Body," *Exp. Fluids*, **56**(6), p. 126.
- [9] Spohn, A., and Gillieron, P., 2002, "Flow Separations Generated by a Simplified Geometry of an Automotive Vehicle," *Proceedings of IUATM Symposium on Unsteady Separated Flows*, Toulouse, France, Apr. 8–12.
- [10] Corallo, M., Sheridan, J., and Thompson, M. C., 2015, "Effect of Aspect Ratio on the Near Wake Flow Structure of an Ahmed Body," *J. Wind Eng. Ind. Aerodyn.*, **147**, pp. 95–103.
- [11] Leclerc, C., 2008, "Réduction de Trainée D'un Véhicule Automobile Simplifié à L'aide du Contrôle Actif Par Jet Synthétique," These de Doctorat. Institut de Mécanique des Fluides de Toulouse, Toulouse, France.
- [12] Fuller, J., and Passmore, M. A., 2014, "The Importance of Rear Pillar Geometry on Fastback Wake Structures," *J. Wind Eng. Ind. Aerodyn.*, **125**, pp. 111–120.
- [13] Gaylard, A., Howell, J. P., and Garry, K. P., 2007, "Observation of Flow Asymmetry Over the Rear of Notchback Vehicles," *SAE Paper No. 2007-01-0900*.
- [14] Gilhorne, B. R., Saunders, J. W., and Sheridan, J., 2001, "Time Averaged and Unsteady Near-Wake Analysis of Cars," *SAE Paper No. 2001-01-1040*.
- [15] Kounenits, C., Bonitz, S., Ljungskog, E., Lofdahl, L., Broniewicz, A., Larsson, L., and Sebben, S., 2016, "Investigation of the Rear-End Flow Structures on a Sedan Car," *SAE Paper No. 2016-01-1606*.
- [16] Wieser, D., Schmidt, H., Müller, S., Strangfeld, C., Nayeri, C., and Paschereit, C., 2014, "Experimental Comparison of the Aerodynamic Behavior of Fastback and Notchback DrivAer Models," *SAE Int. J. Passeng. Cars – Mech. Syst.*, **7**(2), pp. 682–691.
- [17] Bayraktar, I., Landman, D., and Baysal, O., 2001, "Experimental and Computational Investigation of Ahmed Body for Ground Vehicle Aerodynamics," *SAE Paper No. 2001-01-2742*.
- [18] Strachan, R. K., Knowles, K., and Lawson, N. J., 2004, "A CFD and Experimental Study of an Ahmed Reference Model," *SAE Paper No. 2004-01-0442*.
- [19] Guilmineau, E., 2008, "Computational Study of Flow Around a Simplified Car Body," *J. Wind Eng. Ind. Aerodyn.*, **96**(6–7), pp. 1207–1217.
- [20] Krastev, V. K., and Bella, G., 2011, "On the Steady and Unsteady Turbulence Modeling in Ground Vehicle Aerodynamic Design and Optimization," *SAE Paper No. 2011-24-0163*.
- [21] Ashton, N., and Revell, A., 2015, "Key Factors in the Use of DDES for the Flow Around a Simplified Car," *Int. J. Heat Fluid Flow*, **54**, pp. 236–249.
- [22] Serre, E., Minguez, M., Pasquetti, R., Guilmineau, E., Deng, G. B., Kornhaas, M., Schafer, M., Frohlich, J., Hinterberger, C., and Rodi, W., 2013, "On Simulating the Turbulent Flow Around the Ahmed Body: A French-German Collaborative Evaluation of LES and DES," *Comput. Fluids*, **78**, pp. 10–23.
- [23] Krajnovic, S., and Davidson, L., 2004, "Large-Eddy Simulation of the Flow Around Simplified Car Model," *SAE Paper No. 2004-01-0227*.
- [24] Kapadia, S., Roy, S., Vallero, M., Wurtzler, K., and Forsythe, J., 2004, "Detached-Eddy Simulation Over a Reference Ahmed Car Model," *Direct and Large-Eddy Simulation V. ERCOFTAC Series*, In: Friedrich R., Geurts B. J., Métais O., (eds) Vol. 9, Springer, Dordrecht, The Netherlands.
- [25] Guilmineau, E., Deng, G. B., Leroyer, P., Queutey, P., Visonneau, M., and Wackers, J., 2018, "Assessment of Hybrid RANS-LES Formulations for Flow Simulation Around the Ahmed Body," *Comput. Fluids*, **176**, pp. 302–319.
- [26] Hinterberger, C., García-Villalba, M., and Rodi, W., 2004, "Large Eddy Simulation of Flow Around the Ahmed Body," *The Aerodynamics of Heavy Vehicles: Trucks, Buses, and Trains. Lecture Notes in Applied and Computational Mechanics*, In: McCallen R., Browand F., Ross J. (eds), Vol. 19, Springer, Berlin.
- [27] Krajnovic, S., and Davidson, L., 2005, "Flow Around a Simplified Car, Part I: Large Eddy Simulation," *ASME J. Fluids Eng.*, **127**(5), pp. 907–918.
- [28] Minguez, M., Pasquetti, R., and Serre, E., 2008, "High-Order Large-Eddy Simulation of Flow Over the "Ahmed Body" Car Model," *Phys. Fluids*, **20**(9), p. 095101.
- [29] Lehmkuhl, O., Borrell, R., Rodríguez, I., Pérez-Segarra, C. D., and Oliva, A., 2012, "Assessment of the Symmetry-Preserving Regularization Model on Complex Flows Using Unstructured Grids," *Comput. Fluids*, **60**, pp. 108–116.
- [30] Venning, J., Lo Jacono, D., Burton, D., Thompson, M. C., and Sheridan, J., 2017, "The Nature of the Vortical Structures in the Near Wake of the Ahmed Body," *Proc. Inst. Mech. Eng., Part D*, **231**(9), pp. 1239–1244.
- [31] Schmidt, S., Franke, M., and Thiele, F., 2001, "Assessment of SGS Models in LES Applied to a NACA 4412 Airfoil," *39th Aerospace Sciences Meeting and Exhibit, Aerospace Sciences Meetings*, Reno, NV, Jan. 8–11, p. 434.
- [32] Moussaed, C., Wormom, S., Salvetti, M.-V., Koobus, B., and Dervieux, A., 2014, "Impact of Dynamic Subgrid-Scale Modeling in Variational Multiscale Large-Eddy Simulation of Bluff-Body Flows," *Acta Mech.*, **225**(12), pp. 3309–3323.
- [33] Smagorinsky, J., 1963, "General Circulation Experiments With the Primitive Equations: I. The Basic Experiment," *Mon. Weather Rev.*, **91**(3), pp. 99–164.
- [34] Germano, M., Piomelli, U., Moin, P., and Cabot, W. H., 1991, "A Dynamic Subgrid-Scale Eddy Viscosity Model," *Phys. Fluids A: Fluid Dyn.*, **3**(7), pp. 1760–1765.

- [35] Kim, S., 2004, "Large Eddy Simulation Using Unstructured Meshes and Dynamic Subgrid-Scale Turbulence Models," *AIAA Paper No. 2004-2548*.
- [36] Nicoud, F., and Ducros, F., 1999, "Subgrid-Scale Stress Modelling Based on the Square of the Velocity Gradient Tensor," *Flow, Turbl. Combust.*, **62**(3), pp. 183–200.
- [37] Davidson, L., Cokljat, D., Fröhlich, J., Leschziner, M. A., Mellen, C., and Rodi, W., 2003, *LESFOIL: Large Eddy Simulation of Flow Around a High Lift Airfoil: Results of the Project LESFOIL Supported by the European Union 1998–2001*, Vol. 83, Springer, Berlin.
- [38] Caridi, D., Cokljat, D., Schuetze, J., and Lechner, R., 2012, "Embedded Large Eddy Simulation of Flow Around the Ahmed Body," *SAE Int. J. Commer. Veh.*, **5**(1), pp. 208–214.
- [39] Leonard, B., 1991, "The ULTIMATE Conservative Difference Scheme Applied to Unsteady One-Dimensional Advection," *Comput. Methods Appl. Mech. Eng.*, **88**(1), pp. 17–74.
- [40] Jasak, H., Weller, H. G., and Gosman, A. D., 1999, "High Resolution NVD Differencing Scheme for Arbitrary Unstructured Meshes," *Numer. Methods Fluids*, **31**(2), pp. 431–449.
- [41] Menter, F. R., 1994, "Two-Equation Eddy-Viscosity Turbulence Models for Engineering Applications," *AIAA J.*, **32**(8), pp. 1598–1605.
- [42] Piomelli, U., and Chasnov, J. R., 1996, "Large-Eddy Simulations – Theory and Applications," *Turbulence and Transition Modelling*. In: Hallback, M., Henningson, D. S., Johansson, A. V., Alfredson, P. H. (Eds.), Springer, Dordrecht, The Netherlands, pp. 269–336.
- [43] Pope, S., 2004, "Ten Questions Concerning the Large-Eddy Simulation of Turbulent Flows," *New J. Phys.*, **6**, pp. 35–35.
- [44] Fröhlich, J., Mellen, C. P., Rodi, W., Temmerman, L., and Leschziner, M., 2005, "Highly Resolved Large-Eddy Simulation of Separated Flow in a Channel With Streamwise Periodic Constrictions," *J. Fluid Mech.*, **526**, pp. 19–66.
- [45] Davidson, L., 2011, "How to Estimate the Resolution of an LES of Recirculating Flow," *Quality and Reliability of Large-Eddy Simulations II (ERCOTAC Series)*, In: Salvetti M., Geurts B., Meyers J., Sagaut P. (eds), Vol. 16, Springer, Dordrecht, The Netherlands, pp. 269–286.
- [46] Davidson, L., 2009, "Large Eddy Simulations: How to Evaluate Resolution," *Int. J. Heat Fluid Flow*, **30**(5), pp. 1016–1025.
- [47] Fouras, A., Lo Jacono, D., and Hourigan, K., 2008, "Target-Free Stereo PIV: A Novel Technique With Inherent Error Estimation and Improved Accuracy," *Exp. Fluids*, **44**(2), pp. 317–329.
- [48] Graftieaux, L., Michard, M., and Grosjean, N., 2001, "Combining PIV, POD and Vortex Identification Algorithms for the Study of Unsteady Turbulent Swirling Flows," *Meas. Sci. Technol.*, **12**(9), pp. 1422–1429.
- [49] Krajnovic, S., and Davidson, L., 2005, "Flow Around a Simplified Car—Part 2: Understanding the Flow," *ASME J. Fluids Eng.*, **127**(5), pp. 919–928.